nature electronics

Article

https://doi.org/10.1038/s41928-024-01264-3

Light-emitting diodes based on intercalated transition metal dichalcogenides with suppressed efficiency roll-off at high generation rates

Received: 15 August 2023

Accepted: 25 September 2024

Published online: 28 October 2024

Check for updates

Shixuan Wang[1,15], Qiang Fu[1,15], Ting Zheng[1], Xu Han[2], Hao Wang[3], Tao Zhou[1], Jing Liu[1], Tianqi Liu[1], Yuwei Zhang[1], Kaiqi Chen[4], Qixing Wang[5], Zhexing Duan[1], Xin Zhou[6], Kenji Watanabe[7], Takashi Taniguchi[8], Jiaxu Yan[9], Yuan Huang[2], Yuwei Xiong[4], Joel K. W. Yang[3], Zhenliang Hu[1], Tao Xu[4], Litao Sun[4], Jinhua Hong[10], Yujie Zheng[11], Yumeng You[12], Qi Zhang[1] ✉, Junpeng Lu[1,13] ✉ & Zhenhua Ni[1,13,14] ✉

The capabilities of light-emitting diodes (LEDs) based on two-dimensional materials are restricted by efficiency roll-off, which is induced by exciton–exciton annihilation, at high current densities. Dielectric or strain engineering can be used to reduce exciton–exciton annihilation rates in monolayer transition metal dichalcogenides, but achieving electroluminescence in two-dimensional LEDs without efficiency roll-off is challenging. Here we describe pulsed LEDs that are based on intercalated transition metal dichalcogenides and offer suppressed exciton–exciton annihilation at high exciton generation rates. We intercalate oxygen plasma into few-layer molybdenum disulfide (MoS_2) and tungsten disulfide (WS_2) to create LEDs with a suppressed efficiency roll-off in both photo-excitation and electro-injection luminescence at all exciton densities up to around 10^{20} cm^{-2} s^{-1}. We attribute this suppression to a reduced exciton Bohr radius and exciton diffusion coefficient, as extracted from optical spectroscopy measurements. LEDs based on intercalated MoS_2 and WS_2 operate at maximum external quantum efficiencies of 0.02% and 0.78%, respectively, at a generation rate of around 10^{20} cm^{-2} s^{-1}.

Efficiency roll-off limits the performance of light-emitting diodes (LEDs) at high current densities[1,2]. For devices based on two-dimensional (2D) materials, strong quantum confinement and reduced dielectric screening in the active materials[3] result in exciton interactions—particularly exciton–exciton annihilation (EEA)—at high generation rates (G)[4,5], which leads to efficiency roll-off. EEA is an Auger-like recombination process typically observed in excitonic semiconductors at high exciton densities, such that one exciton ionizes another while transferring its energy non-radiatively[4,6]. Density-dependent EEA has also been observed in intrinsic 2D excitonic materials, such as defect-free monolayer transition metal dichalcogenides (1L TMDs), and it leads to a sharp decrease in the quantum yield (QY) at high G (ref. 7).

Efforts have been made to alleviate EEA and the consequent drop in QY at high exciton densities[8,9]. Dielectric engineering can limit non-radiative EEA in excitonic materials, such as through hexagonal boron nitride (hBN) encapsulation[3] and the use of high-κ substrates[10].

A full list of affiliations appears at the end of the paper. ✉e-mail: zhangxinyunqi@seu.edu.cn; phyljp@seu.edu.cn; zhni@seu.edu.cn

Modifying the interactions between excitons and their dielectric surroundings can reduce the number of localized non-radiative recombination centres[11–13], thereby mitigating efficiency roll-off. In addition, as-exfoliated 1L TMDs have been shown to exhibit exacerbated EEA when the van Hove singularity resonance coincides with twice the exciton transition energy[14,15]. In this case, the suppression of EEA in 1L TMDs can also be achieved by applying a tensile strain[16], which shifts the final states of dissociated carriers from the van Hove singularities due to a divergence of the density of states. However, applying a strain causes undesirable changes to the electroluminescence (EL), such as linewidth broadening and intensity unevenness, which are detrimental to both optical communication and display applications. A near-unity photoluminescence quantum yield (PLQY) for G up to around 10^{20} cm^{-2} s^{-1} can be reached by using dielectric engineering or strain to reduce EEA rates in 1L TMDs. However, achieving EL without efficiency roll-off in 2D LEDs remains a challenge.

In this Article, we describe a roll-off-free 2D LED based on plasma-intercalated few-layer TMDs. We fabricated quantum-well-like superlattices using one-step oxygen-plasma intercalation, which delaminated the tightly bound layers and resulted in the stacking of a few quasi-monolayers. This stacking into a hybrid superlattice alters the electronic structure and enhances the photoluminescence (PL). The intercalated few-layer TMDs exhibit a suppressed EEA and a brighter luminescence without efficiency roll-off compared to their pristine monolayer counterparts. The intercalated few-layer TMDs show weakened exciton–exciton interactions with a reduced exciton Bohr radius and exciton diffusion coefficient. We fabricated LEDs based on intercalated trilayer (3L) MoS_2 and WS_2 that work under transient excitations and have a better tolerance to EEA compared to previous devices[17–22]. Our intercalated MoS_2 and WS_2 LEDs operate with an external quantum efficiency (EQE) of up to 0.02% and 0.78%, respectively, at G of around 10^{20} cm^{-2} s^{-1}.

Oxygen-plasma-intercalated TMDs

Figure 1a is a schematic of oxygen-plasma intercalation for few-layer TMDs. The TMD flakes were intercalated and decoupled by the radial movement of oxygen plasma excited in an inductively coupled plasma instrument working in capacitive discharge mode (Supplementary Fig. 1 and Supplementary Note 1)[23]. Figure 1b displays topography images captured by atomic force microscopy (AFM) of MoS_2 flakes taken before and after oxygen-plasma intercalation. We observed an increase in flake thickness. Along the white dashed lines in Fig. 1b, the height of 3L (bilayer, 2L) MoS_2 increased from 2.34 nm (1.68 nm) to 4.61 nm (3.52 nm) due to oxygen-plasma intercalation between adjacent layers. Compared with pristine few-layer MoS_2, the thickness of the intercalated MoS_2 had nearly doubled. This is consistent with previous reports on TMD superlattices fabricated by intercalating O_2^+ ions into the interlayer space[23]. The increase in flake thickness is supported by cross-sectional transmission electron microscopy (TEM) measurements (Supplementary Fig. 2). However, the thickness of the 1L region did not increase after oxygen-plasma intercalation (Supplementary Fig. 3), indicating that the change in thickness in the few-layer regions did not result from oxidation of the topmost atomic layer, which is also supported by the absence of vibrational modes of MoO_x in the Raman spectrum (Supplementary Fig. 4)[24] and negligible Mo^{6+} peak in the X-ray photoelectron spectroscopy (XPS) spectrum (Supplementary Fig. 5)[23]. Moreover, the O 1*s* peak in the XPS spectrum suggests that the intercalated species could be oxygen molecules[25], which is consistent with our density functional theory calculations (Supplementary Fig. 6). Moreover, scanning electron microscopy (SEM) characterization (Supplementary Fig. 7) shows that, unlike the atomically flat pristine few-layer MoS_2 flakes, the few-layer region became swollen after plasma intercalation, which is consistent with the AFM and cross-sectional TEM results that show an increase in the interlayer distance.

PLQY versus generation rate

The interlayer coupling strength of the few layers can be tuned by an interlayer spacer after oxygen-plasma intercalation[23]. Tightly coupled layers were decoupled into stacks of quasi-monolayers, which was accompanied by a notable enhancement in the PL intensity. The PL mapping (Fig. 1c) shows that there was uniform PL enhancement across the intercalated few-layer region. At a consistent pump excitation of 1.51×10^2 W cm^{-2} ($G = 1.67 \times 10^{19}$ cm^{-2} s^{-1}), Fig. 1d shows that the PL emission of the intercalated 3L MoS_2 was enhanced after plasma intercalation, up to 54-fold compared to the pristine 1L MoS_2, whereas the intercalated 2L MoS_2 had a tenfold enhancement compared to the pristine 1L MoS_2. The PL from the intercalated few-layer MoS_2 increased with the number of layers due to the increase in the number of decoupled active layers (Supplementary Fig. 8a), similar as conventional quantum wells, for which encapsulating more emission monolayers increases the luminescence[26]. Note that the PL emission increased in a superlinear manner with thickness. This could be linked to the emission layers of a thicker flake being less influenced by the SiO_2/Si substrate, which usually diminishes the PL, thus modifying the exciton recombination dynamics. Moreover, 3L intercalated MoS_2 has a lower defect concentration than the 2L counterpart (Supplementary Figs. 11 and 12), which may also contribute to the enhanced PL emission. Furthermore, Fig. 1d shows that the PL peaks exhibited a redshift around 30 meV as the number of layers increased, which could be a result of enhanced dielectric screening and tensile strain[26]. Additionally, the indirect bandgap emission almost disappeared, whereas the direct bandgap emission was greatly enhanced after intercalation (Supplementary Fig. 8b), which is consistent with the formation of quasi-monolayer structures due to the intercalation and decoupling between adjacent layers[27].

The enhancement of PL from intercalated MoS_2 flakes is also supported by studies of representative back-gated field-effect transistors (FETs) (Fig. 1e). The transfer characteristics of the FET devices as well as the hysteresis (Supplementary Fig. 9a) were analysed during the staged treatment, which revealed a doping shift from the native n-type (stage 1) to a more n-type state (stage 2), followed by a shift towards a p-type state (stage 3), ultimately achieving a neutral state with greatly enhanced PL (stage 4). The corresponding PL spectra at different stages are shown in Supplementary Fig. 9b. Kelvin probe force microscopy (KPFM) was used to characterize the surface potential of pristine and intercalated samples, which confirmed the doping transition (Supplementary Fig. 10).

To gain a deeper understanding of the intercalation process and doping shift, scanning transmission electron microscopy (STEM) measurements were performed on 3L MoS_2 samples at the four stages (Fig. 1e). The atomic defect density increased from 2.6×10^{11} cm^{-2} to 3.5×10^{12} cm^{-2} during the intercalation. The dominant defect type was a single sulfur vacancy, which can cause n-type doping (Supplementary Fig. 11). Similar behaviour was also observed in 2L MoS_2 samples (Supplementary Fig. 12). As oxygen-plasma intercalation eventually enables p-type doping in intrinsically n-doped MoS_2, the intercalation process could be done in two steps. First, the plasma was used to remove surface adsorbates and pollutants. This caused minor damage to the topmost layer although the underlying MoS_2 was still intact. This is evidenced by the shift in the transfer curve together with the reduced transconductance near the onset, which corresponds to the transport behaviour of the topmost MoS_2 layer with a higher n-doping level (stage 2 in Fig. 1e). Second, as the oxygen plasma gradually intercalated into the interlayer gap and expanded the interlayer space, p-doping became dominant by modifying, filling and passivating the sulfur vacancy defects[28,29]. Finally, the intercalation process concluded, and tightly bound layers were delaminated into few quasi-monolayers separated by intercalated oxygen molecules as spacers. The hybrid superlattices behave as a neutral doping material with notable PL enhancement. The oxygen-plasma doping shifted the Fermi level to the middle of the bandgap, and the luminescence came more from neutral exciton recombination.

https://doi.org/10.1038/s41928-024-01264-3

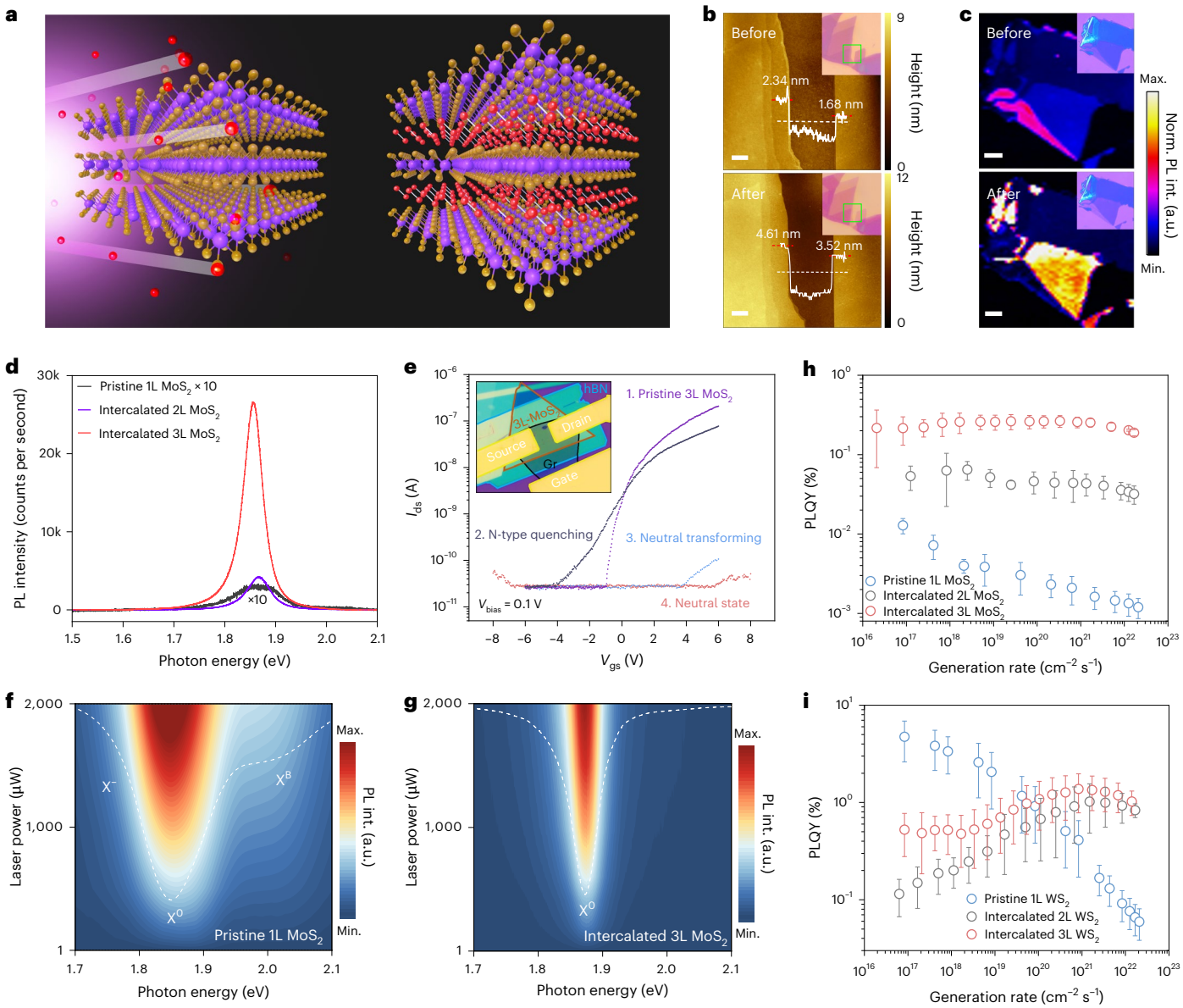

Fig. 1 | Oxygen-plasma intercalation. a, Schematic illustration of oxygen-plasma intercalation into few-layer MoS_2 flakes. The red, yellow and purple atoms represent oxygen, sulfur and transition metal atoms, respectively. **b**, AFM topography images of MoS_2 flakes taken before and after the oxygen-plasma intercalation. Along the dashed white lines, the left region is 3L MoS_2 whereas the right counterpart is 2L MoS_2. Insets, corresponding optical images. **c**, PL maps of few-layer MoS_2 flakes before and after the oxygen-plasma intercalation. Insets, corresponding optical micrographs. **d**, PL spectra of pristine 1L MoS_2 (multiplied by 10) and intercalated 2L and 3L MoS_2 flakes measured at an incident power of 1.51×10^2 W cm^{-2} ($G = 1.67 \times 10^{19}$ cm^{-2} s^{-1}). **e**, Transfer characteristics of a back-gated FET during staged plasma treatment. The current I_{ds} is plotted as a function of gate voltage V_{gs} on a logarithmic scale at a fixed bias voltage of $V_{bias} = 0.1$ V. Inset, corresponding optical image. **f**,**g**, Contour maps of the power-dependent PL spectra as a function of excitation power, which was varied from 1 to 2,000 μW in pristine 1L MoS_2 (**f**) and intercalated 3L MoS_2 (**g**). The white dashed lines represent the PL spectra of the corresponding samples at an incident power of 1.51×10^5 W cm^{-2}. X^0 represents a neutral exciton, X^- a charged exciton and X^B a B exciton from a higher-lying excitonic transition. **h**,**i**, PLQY of MoS_2 flakes (**h**) and WS_2 flakes (**i**) versus G for excitons. The error bars for δPLQY are standard deviations based on the differences between samples: $\delta\mathrm{PLQY} = \sqrt{\frac{\sum_{i=1}^{n}(\mathrm{PLQY}_i - \overline{\mathrm{PLQY}})^2}{n-1}}$, where $\overline{\mathrm{PLQY}}$ and n are the average PLQY of the samples and the number of samples, respectively. int., intensity; max., maximum; min., minimum; norm., normalized. Scale bars, 1 μm (**b**), 5 μm (**c**).

Power dependency of the PL was analysed to explore the performance of the plasma-intercalated MoS_2 flakes, especially at high G. In contrast with the observed peak broadening (full-width at half-maximum, FWHM, around 101 meV) of pristine 1L MoS_2 (Fig. 1f), the intercalated 2L and 3L MoS_2 retained a single neutral exciton peak (X^0) with a smaller linewidth (around 52 meV) as the excitation power was varied from 1 to 2,000 μW (Fig. 1g and Supplementary Fig. 13). The absence of a charged exciton peak (trion, X^-) and a higher-energy excitonic transition (B exciton, X^B) for the intercalated MoS_2 also suggests that the hybrid superlattice formed by intercalation had a better sample quality with fewer defects and trap centres and had a negligible number of redundant electronic states in the bandgap, which is consistent with the results for the FETs (Fig. 1e). For corresponding results of WS_2, see Supplementary Fig. 14.

At high G, the PLQY of pristine 1L MoS_2 rolled off due to EEA (Fig. 1h), but the PLQY drop-off in pristine few-layer MoS_2 was mitigated due to the weakened quantum confinement and strengthened dielectric screening, which benefited from the adjacent layers (Supplementary

https://doi.org/10.1038/s41928-024-01264-3

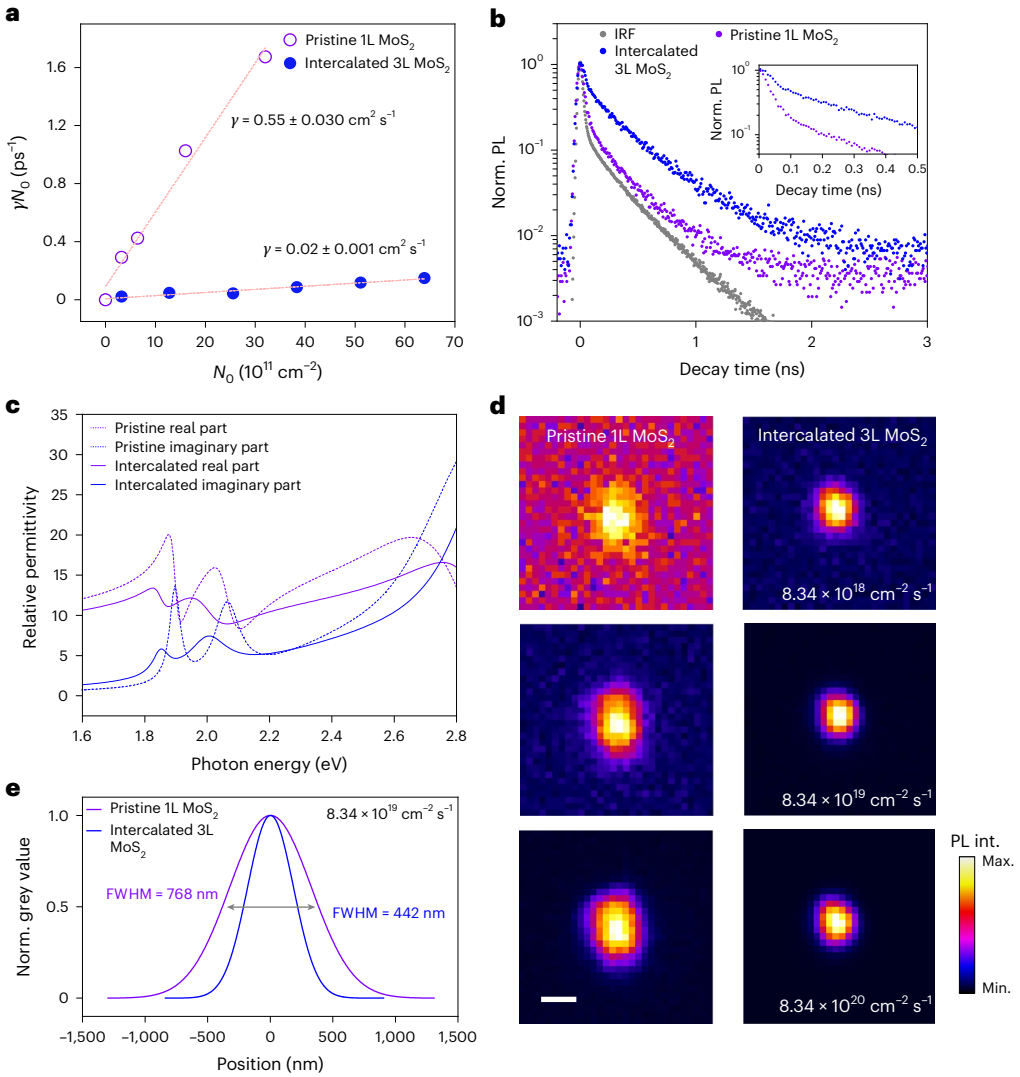

Fig. 2 | Mechanism for EEA suppression. a, EEA rates calculated from optical pump–probe measurements. γN_0 is shown as a function of N_0. The slope γ was obtained for pristine 1L and intercalated 3L MoS_2 flakes. N_0 is the initially injected exciton density at $t = 0$, and γ is the EEA rate constant. The red dashed lines are linear fits to the data. **b**, TRPL decay of pristine 1L MoS_2 and intercalated 3L MoS_2 at $G = 2.08 \times 10^{19}$ cm^{-2} s^{-1}, as well as the instrument response function (IRF). Inset, TRPL curves over a short period of time. **c**, Real and imaginary parts of the relative permittivity of few-layer MoS_2 flakes taken before and after the plasma intercalation. **d**, Spatial images of PL signals for pristine 1L MoS_2 and intercalated 3L MoS_2 at various G values. Images in the same row were captured under the same pump power, and those in the same column were for the same sample. **e**, Radial intensity profiles of the exciton diffusion images at $G = 8.34 \times 10^{19}$ cm^{-2} s^{-1}, revealing narrowed broadening for intercalated 3L MoS_2. Scale bar, 800 nm.

Fig. 15a,b). No PLQY drop-off was observed in intercalated 3L MoS_2 at all G up to 6.67×10^{21} cm^{-2} s^{-1} (Fig. 1h). For the intercalated 2L MoS_2, the PLQY droop did not emerge until G reached 1.67×10^{21} cm^{-2} s^{-1}. Notably, by applying a tensile strain[14], the PLQY drop-off in 1L TMDs was inhibited at G below 10^{20} cm^{-2} s^{-1}. Thus, the few-layer TMDs prepared by plasma intercalation were more resistant to efficiency roll-off than the strained monolayers. Because there was no decrease in the PLQY at high G, the PLQY of the intercalated 3L MoS_2 was much higher, by two orders of magnitude, than that of the pristine 1L MoS_2. As for intercalated few-layer MoS_2, the absence of a PLQY roll-off was also observed in plasma-intercalated WS_2 flakes (Fig. 1i). Instead of the sharp downward trend observed in pristine 1L WS_2, the PLQY of intercalated few-layer WS_2 increased with G from 10^{17} to 10^{21} cm^{-2} s^{-1}, which can be understood as the depletion of redundant carriers (Supplementary Fig. 15c,d). As the excitation power was increased, the trion concentration reached saturation with the total charge concentration, beyond which excitons lacked excess background carriers to form trion and trigger non-radiative recombination (Supplementary Fig. 16). The neutral exciton recombination pathway then dominated, which increased the QY until EEA became dominant. An analogous QY upswing has also been observed in pristine 1L WS_2 and electrostatically doped 1L WSe_2 (refs. 30,31). A benchmark of PLQY as a function of generation rate is also provided in Supplementary Fig. 17.

Mechanism for suppressing EEA

In excitonic semiconductors, EEA is primarily responsible for the PLQY roll-off[14]. Therefore, we surveyed the PLQY without roll-off for intercalated layers from the perspective of EEA. To clarify the dynamics of EEA in the intercalated layers, we performed optical pump–probe measurements on both as-exfoliated and plasma-intercalated TMD flakes. Differential reflection signals as a function of injected carrier density measured from regions of MoS_2 and WS_2 flakes are shown in Supplementary Fig. 18. The exciton density at high G evolves as[32,33]:

$$N_0/N_t - 1 = \gamma N_0 t \quad (1)$$

https://doi.org/10.1038/s41928-024-01264-3

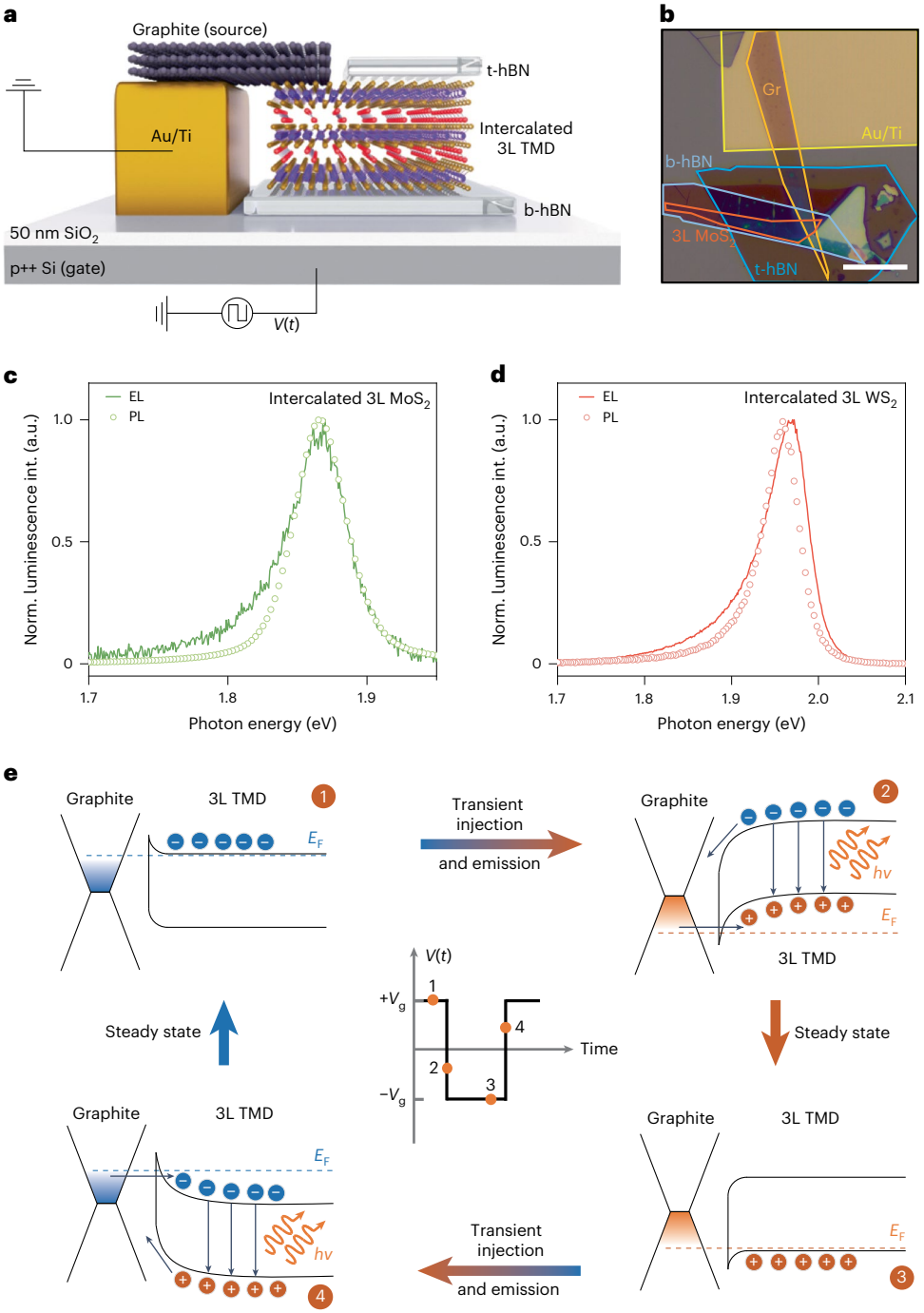

Fig. 3 | Transient 2D LEDs based on intercalated 3L TMDs. a, Schematic illustration of the transient 2D LEDs based on intercalated 3L TMD. **b**, Optical microscope image of a typical 2D LED based on intercalated 3L MoS_2. Intercalated 3L MoS_2, top hBN (t-hBN), back hBN (b-hBN), graphite (Gr) and Au/Ti electrodes are denoted by orange, blue, dark blue, dark yellow and yellow, respectively. **c**,**d**, EL spectra of 2D LEDs based on intercalated 3L MoS_2 (**c**) and intercalated 3L WS_2 (**d**) working under 4 MHz excitation with V_g = 14 *V* and 12 *V*, respectively. EL signals were captured at the proximity of the graphite contact. **e**, Band diagram of transient EL. Pulsed EL was created at phases 2 and 4 only when the voltage shifted up or down. In the centre inset, the applied square wave V_g (gate voltage) is a function of time and the denoted 1, 2, 3 and 4 correspond to the different phases. E_F and *hv* stand for the Fermi level and the photon energy, respectively. Scale bar, 15 µm.

where N_t is the exciton density, N_0 is the initially injected exciton density at $t = 0$ and γ is the annihilation rate constant. A series of γN_0 values were extracted (Supplementary Fig. 18) and then plotted as a function of N_0 in Fig. 2a. The EEA rate of the intercalated 3L MoS_2 (0.02 ± 0.001 cm^2 s^{-1}) is one order of magnitude lower than that of the pristine 1L MoS_2 (0.55 ± 0.030 cm^2 s^{-1}), which further demonstrates the weaker effect of EEA in the oxygen-plasma-intercalated layers.

The time-resolved photoluminescence (TRPL) was also measured to investigate the dynamics of carrier recombination (Fig. 2b and Supplementary Fig. 19). The annihilation rate was determined from the luminescence decay curves (Supplementary Fig. 20). Intercalated 3L MoS_2 had an overall longer lifetime than that of pristine 1L MoS_2, which also indicates the reduced EEA[31]. The EEA rate of WS_2 is shown in Supplementary Fig. 21.

https://doi.org/10.1038/s41928-024-01264-3

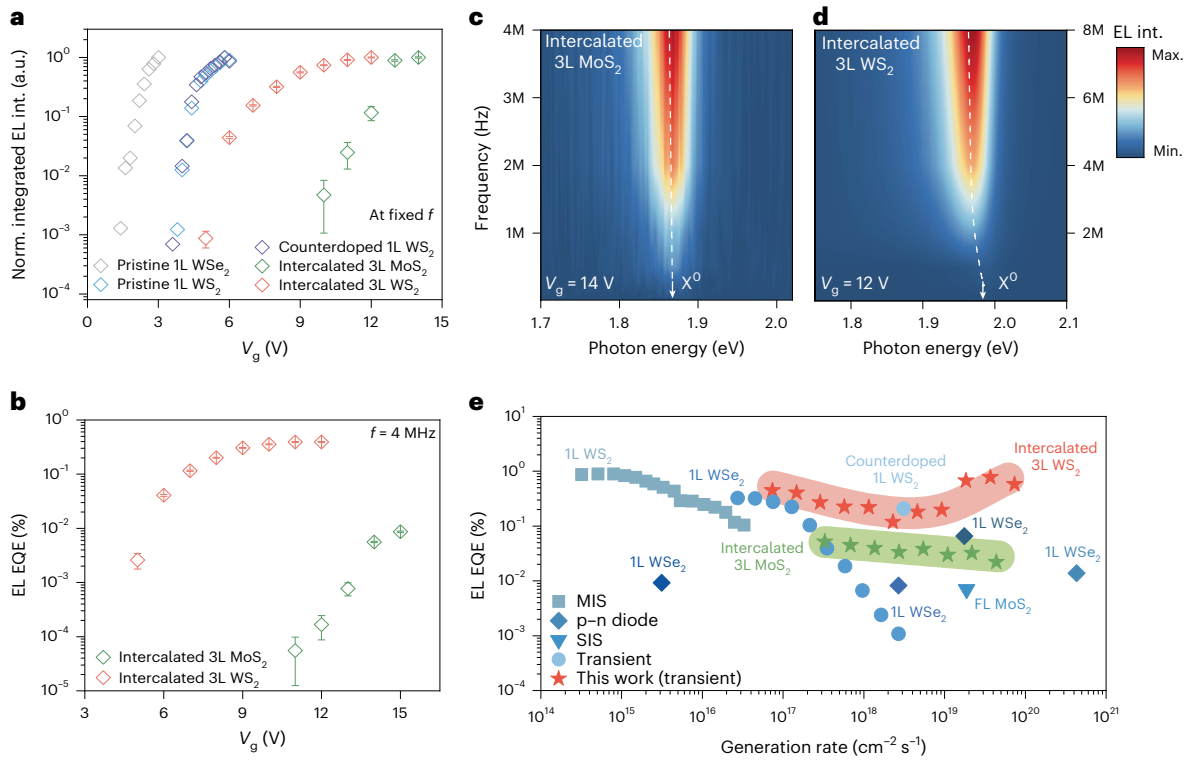

Fig. 4 | EL EQE of transient 2D LEDs based on intercalated 3L MoS_2 and WS_2. **a**, Normalized EL integrated intensity of 2D LEDs based on intercalated 3L MoS_2 (green), intercalated 3L WS_2 (orange), pristine 1L WSe_2 (grey), pristine (blue) and counterdoped 1L WS_2 (purple) as a function of V_g at a fixed modulation frequency. The integrated intensities of the latter three devices were extracted from previous reports[17]. The error bar is based on the measurement uncertainties. **b**, EL EQE of 2D LEDs based on intercalated 3L MoS_2 (green) and intercalated 3L WS_2 (orange) as a function of V_g under 4 MHz excitation. The error bar is based on the measurement uncertainties. **c**,**d**, Contour maps of EL intensity as a function of modulation frequency for intercalated 3L MoS_2 (**c**) and intercalated 3L WS_2 (**d**). Both sets of EL values are dominated by neutral exciton X^0 emission. **e**, Benchmark of the EL EQE of 2D LEDs as a function of G. Devices based on intercalated few-layer TMDs show evident edges at high exciton densities compared to other devices, including p–n junctions[18,19,22,50], metal–insulator–semiconductors (MIS)[20], semiconductor–insulator–semiconductors (SIS)[21] and other transient 2D LEDs[17,51]. FL, few layer.

Generally, the larger the exciton Bohr radius is, the larger the exciton diffusion coefficient is, and the greater the probability of one exciton ionizing another exciton will be[11,34]. We performed in situ optical reflection and transmission measurements on few-layer MoS_2 and WS_2 samples before and after plasma intercalation and modelled their corresponding dielectric functions (Supplementary Fig. 22). As shown in Fig. 2c, the permittivity in the visible range for intercalated layers was smaller than that of before intercalation. It was also smaller than the previously reported permittivity of 1L MoS_2 and WS_2 (ref. 35). Under strong quantum confinement, such as in 2D materials, the exciton Bohr radius r_e is positively correlated with the dielectric value[36]:

$$r_e = \frac{\varepsilon\hbar^2}{e^2}\left(\frac{1}{m_e} + \frac{1}{m_h}\right), \quad (2)$$

where ε is the dielectric constant, $\hbar$ is the reduced Planck constant, e is the electron charge, and m_e and m_h are the effective masses of electrons and holes, respectively. According to equation (2), a smaller dielectric value corresponds to a smaller exciton Bohr radius. Moreover, the exciton diffusion properties of pristine 1L and intercalated 3L MoS_2 were investigated by spatial imaging (using a charge-coupled device, CCD) of PL signals taken at various G values (Fig. 2d). These images show that exciton propagation driven by EEA in intercalated 3L MoS_2 (FWHM = 442 nm; Fig. 2e) was suppressed in contrast to pristine 1L MoS_2 (FWHM = 768 nm). Usually, the annihilation of an exciton increases the kinetic energy of a nearby exciton, which allows it to propagate further, resulting in a large diffusion pattern[34]. However, oxygen-plasma-intercalated 3L MoS_2 has a shorter diffusion length and fewer charged excitons accumulate in the patterns, which is consistent with the results in Fig. 1f,g[34]. The exciton diffusion length l is defined as the mean radius of the diffusion map deconvolved by the excitation laser spot size. We obtained the exciton diffusion coefficient D from $l = \sqrt{D\tau}$ (refs. 10,34). τ is the exciton lifetime.

In contrast to pristine 1L MoS_2, the intercalated 3L MoS_2 had an elongated recombination lifetime (Fig. 2b and Supplementary Fig. 19) as well as a reduced exciton diffusion length (Fig. 2e). These factors contributed to the notable decrease in the exciton diffusion coefficient. When G reached 8.34×10^{19} cm^{-2} s^{-1}, the diffusion coefficient (for the calculation details, see Supplementary Fig. 23 and Supplementary Note 4) of intercalated 3L MoS_2 (0.02 cm^2 s^{-1}) was one order of magnitude lower than that of the pristine 1L MoS_2 (0.51 cm^2 s^{-1}), consistent with previous reports[37], which indicates the weakened EEA in the intercalated layers. Note that the intercalation resulted in lattice strain, as evidenced by the cross-sectional TEM and SEM results, and this may also contribute to the suppression of EEA[14]. Unlike the prominent exciton interactions in pristine monolayers, the many-body excitonic interactions in intercalated layers were much weaker, which was synergistically corroborated by the smaller exciton Bohr radius and exciton diffusion coefficient, as well as possible contributions from the lattice strain, which thereby effectively suppressed EEA.

Intercalated few-layer TMD LEDs

Based on the suppressed EEA at high exciton densities and to demonstrate the potential of the intercalated few-layer MoS_2 and WS_2 in light-emitting applications, transient 2D LEDs working under square-wave modulation were fabricated using the intercalated 3L

MoS_2 and WS_2 as active layers because of their higher PLQY compared to their 2L counterparts. A schematic and optical image are shown in Fig. 3a,b, respectively. To slow down degradation of the active materials under ambient conditions, the devices were encapsulated by hBN flakes after oxygen-plasma intercalation. Few-layer graphene was selected as the source contact on the active layer because of its van der Waals-type electrical contact and lower contact resistance[17]. Both intercalated 3L MoS_2 and WS_2 demonstrated prominent EL near the graphene contact region (Fig. 3c,d)[17,30]. Their EL mainly originated from the respective neutral exciton X^0 emissions located at around 1.86 eV (MoS_2) and around 1.98 eV (WS_2), similar to their PL spectra.

Figure 3e shows a cycle of the square wave applied to the devices. Four typical phases are denoted. When $+V_g$ was applied between the source and gate electrodes (phase 1 in Fig. 3e), the Fermi level of graphene was lifted above its Dirac point, which resulted in electrons accumulating in the active material. The entire system was in a steady state. When $+V_g$ instantaneously shifted to $-V_g$ (phase 2 in Fig. 3e), electrons immediately drifted off from the active material whereas holes tunnelled into it because of the sharp band bending near the contact region. Therefore, pulsed EL was observed near the contact region where electrons and holes encountered each other to form excitons and recombine radiatively[17]. Due to their relatively lower PLQY, pristine and moderately intercalated 3L MoS_2 exhibited no observable EL in our experiments. However, a transition from an indirect exciton-dominant state to a direct neutral-exciton-dominant state (Supplementary Fig. 24a) was observed for 3L WS_2, which implies the continuous weakening of interlayer coupling and improvement of PLQY by oxygen-plasma intercalation.

To examine the EEA-related events at high G, the V_g-dependent EL features of our intercalated samples were analysed. As charge carriers were injected and retracted during the voltage transition within a duration τ around 6 ns (square-wave transition delay), the average generation rate $\bar{G}$ per transition was approximated by:

$$\bar{G} = \frac{n_0 + p_0}{2\tau} = \frac{C_{ox+hBN}(2V_g - E_g/q)/q}{2\tau} \quad (3)$$

where $n_0 + p_0$, C_{ox+hBN}, E_g and q correspond to the number of injected carriers per cycle, the areal capacitance of the device, the electronic bandgap of the active material and the elementary charge, respectively[17,38]. Saturation of both EL intensity and EQE will emerge in transient 2D LEDs if they are driven by a sufficiently high V_g because of EEA events[17,38]. Figure 4a,b shows the V_g-dependent EL integrated intensity and EQE of our intercalated 3L samples and intrinsic 1L samples at a fixed modulation frequency (4 MHz). The EL of fully intercalated 3L MoS_2 and WS_2 was observed for V_g higher than 11 V and 5 V, respectively. The substantial difference in the threshold voltages of intercalated MoS_2 and WS_2 resulted from the much lower EL EQE of MoS_2, which required a higher excitation level for the spectrometer to perceive the EL signals. Because of the increasingly enhanced EEA at higher V_g, a continuous decrease in the slope of the semilogarithmic integrated intensity versus V_g diagram was observed in intercalated 3L WS_2 (ref. 39). The EL intensity and EQE saturated at $V_g = 12$ V, which corresponded to an average generation rate $\bar{G}$ of around 8×10^{20} cm^{-2} s^{-1}. For the intercalated 3L MoS_2, neither the EL intensity nor EQE were saturated at $V_g = 14$ V and $\bar{G}$ of around 1.25×10^{21} cm^{-2} s^{-1}. However, further tests were limited by the stability and durability of the active material and oxide at high V_g. In comparison with previous reports[17] (Fig. 4a), the EL of both intrinsic and counterdoped 1L WS_2 saturated at a V_g of around 5.5 V and $\bar{G}$ of around 3.50×10^{20} cm^{-2} s^{-1}. Our intercalated samples demonstrated reduced EEA rates at high carrier generation regimes because of the screened exciton interactions. Additionally, in contrast to pristine 3L WS_2, the EQE of the intercalated 3L WS_2 was enhanced by more than two orders of magnitude under $V_g = 12$ V due to the oxygen-plasma intercalation (Supplementary Fig. 24b), which conformed with the enhancement of the PLQY.

Furthermore, we explored the frequency dependence of EL and EQE at a fixed V_g (14 V and 12 V for MoS_2 and WS_2, respectively) to investigate the performance of our devices. In transient 2D LEDs, changes in the modulation frequency (f) when it was below 50 MHz typically had a negligible impact on the EL EQE due to the nature of the square-wave excitation[17]. Each cycle of carrier injection and pulse emission can, to some degree, be treated independently because the duration between V_g transitions was much longer than the pulsed EL lifetime (less than 10 ns)[17,39]. The EL from the intercalated 3L MoS_2 and WS_2 became observable at around 32 kHz and 8 kHz, respectively. The intensity continuously increased with modulation frequency (Fig. 4c,d). A redshift in the EL from intercalated WS_2 was observed as f was increased, which was attributed to thermal accumulation. Figure 4e displays a benchmark of EL EQE of typical 2D LEDs based on TMDs as a function of G, which in our case is given by $G = f(n_0 + p_0)$ (ref. 17). For intercalated 3L MoS_2, the increase in modulation frequency resulted in a higher integrated EL intensity but a slight decrease in EQE from 0.05 % to 0.02%, which was probably due to the RC delay[40]. The EQE of our 3L intercalated MoS_2 is one of the highest EL EQEs reported for transient MoS_2 devices to date. The EQE is comparable to that of a previously reported transient device based on pristine 1L WSe_2 at a G of approximately mid-10^{17} cm^{-2} s^{-1} (ref. 15). At a higher injection rate of approximately mid-10^{18} cm^{-2} s^{-1}, the EL EQE of the 3L intercalated MoS_2 was almost two orders of magnitude higher than that of 1L WSe_2 (ref. 15). Unlike the intercalated 3L MoS_2, a peculiar rise of the EL EQE from 0.20% to 0.78% as the frequency was increased from 1 to 4 MHz was observed during stage 3 for 3L WS_2. This is one of the highest EQEs ever achieved for transient devices based on 2D semiconductors. It probably was the result of carrier redistribution from lower-energy dark exciton states to higher-energy bright exciton states in tungsten-based active materials due to heat accumulation during device operation, which is elusive in MoS_2 because of the opposite alignment of bright and dark exciton states in the K and K' valleys[41,42]. Additionally, the intercalated 3L WS_2 also had a comparable EQE, even at a G more than five orders of magnitude higher than that of metal–insulator–semiconductor devices based on 1L WS_2 (ref. 20). Our results clearly indicate that due to the high PLQY and immunity to EEA, intercalated 3L MoS_2 and WS_2 have huge potential in the fabrication of next-generation highly luminescent micro-LEDs. Additionally, as our devices can endure a modulation frequency of up to 8 MHz in ambient conditions, they may have promising prospects for ultrafast internal modulated LEDs for on-chip optical interconnect applications, if carefully encapsulated in vacuum.

Conclusions

We have described LEDs based on oxygen-plasma-intercalated few-layer TMDs. The EEA in 3L intercalated MoS_2 was suppressed and exhibited bright luminescence with finite non-radiative recombination centres. Note that the many-body excitonic interactions in a few-layer sample can be tuned by oxygen-plasma intercalation, as illustrated by the decreasing exciton Bohr radius and exciton diffusion coefficient. Photo-excitation and electro-injection luminescence without an efficiency roll-off was achieved at a high G of around 10^{20} cm^{-2} s^{-1}, leading to an EQE of up to 0.02% for transient MoS_2 LEDs.

Methods

Oxygen-plasma intercalation

Few-layer MoS_2 and WS_2 flakes were mechanically exfoliated onto a 300 nm SiO_2/Si substrate from corresponding bulk crystals (HQ Graphene). The flakes were intercalated by oxygen plasma in a home-built planar low-frequency (0.5 MHz) inductively coupled plasma instrument. A sample was placed around 10 cm away from a radio-frequency antenna, and the input radio-frequency power was kept at 80 W. The ambient pressure in the cavity was kept at 18 Pa by introducing O_2 as

a precursor gas with a flow rate of 5 sccm. During the oxygen-plasma intercalation process, we rotated the sample stage to ensure uniform intercalation. For more details, see Supplementary Note 1.

Structural characterization

The AFM topography measurements were carried out with a Bruker Dimension ICON system in tapping mode. SEM topography was measured by an FEI INSPECT F50 system with 20 kV accelerating voltage. Cross-sectional TEM slices of samples were obtained with a Thermo Scientific Helios 5 CX FIB system. Specifically, before bombardment by the ion beam, a 100 µm protective layer of Au was transferred onto an intercalated few-layer sample and a 1 µm protective layer of platinum was deposited onto the target region. Then the target region was cut into thick slices by a gallium-ion beam (0.23–9.3 nA, 30 kV accelerating voltage). Afterwards, the thick slice was transferred onto a half-grid using a micro-manipulator and thinned down to <50 nm using a gallium-ion beam (41–790 pA, 2–8 kV accelerating voltage) to form an ultra-thin slice for the STEM and TEM observations. The TEM observations were performed by an FEI Titan 80–300 system (300 kV acceleration voltage). To identify surface atomic defects, a few-layer sample was transferred directly onto a TEM grid (silicon nitride, 5 µm hole) using polydimethylsiloxane (PDMS). STEM images were then captured by a Thermo Scientific Themis Z system (60 kV accelerating voltage).

Spectroscopic characterization

Optical images were captured by an optical microscope (Leica 4000M). XPS spectra were acquired using a custom-built PREVAC XPS-2 system (photon energy, 1,486.8 eV and pass energy of the analyser, 200 eV). KPFM measurements were made by a MFP-3D Origin (Oxford) in ambient conditions immediately after a sample was prepared. Freshly cleaved, highly oriented pyrolytic graphite was used as a reference. The PL was measured by a Horiba HR320 system with an excitation wavelength of 532 nm and power of 30 µW. The TRPL was measured using a femtosecond laser pulsed at an 80 MHz repetition rate as the photo-excitation source (Coherent, Chameleon Ultra Ti:Sapphire laser). The time-correlated single-photon counting system employed was PicoHarp 300. Transient differential reflection spectra were measured by a home-built optical system with an 80 MHz and 100 fs Ti:sapphire oscillator (the one used for the TRPL measurements), an optical parametric oscillator (Thorlabs), a supercontinuum generator (Thorlabs) and a second-harmonic generator (Thorlabs). For the measurements, two outputs of 400 nm and 615–680 nm were used as the pump and probe pulses, respectively. All measurements were carried out at room temperature under ambient conditions. Details of the PLQY, EEA rate and exciton diffusion imaging measurements are provided in Supplementary Notes 2, 4 and 5.

Theoretical calculations

The permittivity of layered MoS_2 and WS_2 reported here was fitted using an in-house code. First, a modified Lorentz–Drude model was employed to represent the dispersive property of the material, in which the resonance frequency, oscillator strength and damping coefficient of the oscillators were not fixed. Then, the permittivity was fed into a transfer-matrix algorithm, where the sample configuration was set to be the same as in the experiments. The calculated absorption, reflection and transmission spectra were compared with the measured spectra to facilitate the determination of the parameters in the Lorentz–Drude model. After several optimization iterations, the difference between the calculated and measured spectra was minimized. The parameters for the permittivity were then fixed, and the corresponding permittivity and refractive index were obtained.

The density functional theory calculations were performed with the VASP code[43,44] using the projector-augmented plane wave approach and a kinetic energy cutoff of 520 eV. The generalized gradient approximation with the Perdew–Burke–Ernzerhof exchange-correlation functional[45] was employed in all calculations. Grimme's D3 correction[46] was used to consider the van der Waals interactions. Three layers of MoS_2 with a vacuum thickness larger than 15 Å were used to model the intercalation of O_2 molecules and O atoms (Supplementary Fig. 6a). Self-consistent field energy and force convergence criteria were set as 10^{-6} eV and 0.005 eV. Monkhorst–Pack k-grid sampling of $12 \times 12 \times 1$ and $6 \times 6 \times 1$ were used to optimize the $1 \times 1 \times 1$ and $2 \times 2 \times 1$ supercell geometries.

FET characterization

Fabrication of a back-gated FET started with the sequential dry transfer of the graphene gate electrode, hBN dielectric and multilayer TMDs with a PDMS-assisted transfer technique[47]. A three-terminal electrode covered with poly(methyl methacrylate) that had been prefabricated onto a silicon substrate was picked up with PDMS, transferred onto the graphene/hBN/TMD stack and then annealed at 180 °C for 10 min to enhance the interactions between the electrodes and 2D layers. The entire device was then immersed in acetone and isopropyl alcohol to remove the poly(methyl methacrylate) on top. Bonding pads were connected to the pins in a chip carrier by a wire bonder. Electrical characterization was carried out under ambient conditions using a semiconductor parameter analyser (4200A-SCS, Keithley).

Transient EL device characterization

Au/Ti (25 nm/25 nm) contacts were prepatterned onto heavily p-doped 50 nm SiO_2/Si substrates. Bulk crystals of graphite and TMDs were purchased from HQ Graphene. High-quality hBN crystals were provided by Takashi Taniguchi and Kenji Watanabe. Graphite, hBN and multilayer TMDs were mechanically exfoliated with Scotch tape and transferred onto PDMS tape. The number of layers in multilayer TMDs was identified by optical contrast and PL spectra. B-hBN, multilayer TMDs and graphite were sequentially transferred onto the target positions by dry transfer[48,49]. Graphite was used to bridge the Au pad and active materials and was chosen to be neither too thick (low drift mobility) nor too thin (high resistance at the edge of Au pads). Then, the device was brought into the chamber for the oxygen-plasma intercalation treatment. After that, the device was post-baked in a nitrogen-filled glovebox at 180 °C for 1 h to enhance the contact between layers. After fabrication, the devices were attached to chip carriers by conductive adhesive, and a wire bonder was used to bridge the Au pads and pins. Square-wave signals were applied by a RIGOL function generator. Two channels of square-wave signals with the same ground with $V_{pp} = V_g$ and π phase difference were applied to both the Au pad and Si, which was equivalent to a square wave with $V_{pp} = 2V_g$ applied to the Si gate while the Au pad was grounded. This was used to overcome the voltage limit of the function generator. The EL from the transient LEDs was collected in a home-built EL collection system. For details of the EL EQE, see Supplementary Note 3.

Data availability

Source data are provided with this paper. Other data that support the findings of this study are available from the corresponding author upon reasonable request.

References

1. Krames, M. R. et al. Status and future of high-power light-emitting diodes for solid-state lighting. *J. Disp. Technol.* **3**, 160–175 (2007).
2. Murawski, C., Leo, K. & Gather, M. C. Efficiency roll-off in organic light-emitting diodes. *Adv. Mater.* **25**, 6801–6827 (2013).
3. Hoshi, Y. et al. Suppression of exciton-exciton annihilation in tungsten disulfide monolayers encapsulated by hexagonal boron nitrides. *Phys. Rev. B* **95**, 241403 (2017).
4. Wang, F., Wu, Y., Hybertsen, M. S. & Heinz, T. F. Auger recombination of excitons in one-dimensional systems. *Phys. Rev. B* **73**, 245424 (2006).

5. Yu, Y. et al. Fundamental limits of exciton-exciton annihilation for light emission in transition metal dichalcogenide monolayers. *Phys. Rev. B* **93**, 201111 (2016).
6. Kajino, Y. et al. Quantized exciton-exciton annihilation in monolayer WS_2 on $SrTiO_3$ substrate with atomically flat terraces. *Phys. Rev. B* **103**, L241410 (2021).
7. Amani, M. et al. Near-unity photoluminescence quantum yield in MoS_2. *Science* **350**, 1065–1068 (2015).
8. Kumar, S. et al. Exciton annihilation in molecular aggregates suppressed through quantum interference. *Nat. Chem.* **15**, 1118–1126 (2023).
9. Sortino, L. et al. Radiative suppression of exciton–exciton annihilation in a two-dimensional semiconductor. *Light Sci. Appl.* **12**, 202 (2023).
10. Goodman, A. J. et al. Substrate-dependent exciton diffusion and annihilation in chemically treated MoS_2 and WS_2. *J. Phys. Chem. C* **124**, 12175–12184 (2020).
11. Zipfel, J. et al. Exciton diffusion in monolayer semiconductors with suppressed disorder. *Phys. Rev. B* **101**, 115430 (2020).
12. Lee, Y. et al. Boosting quantum yields in two-dimensional semiconductors via proximal metal plates. *Nat. Commun.* **12**, 7095 (2021).
13. Rhodes, D., Chae, S. H., Ribeiro-Palau, R. & Hone, J. Disorder in van der Waals heterostructures of 2D materials. *Nat. Mater.* **18**, 541–549 (2019).
14. Kim, H., Uddin, S. Z., Higashitarumizu, N., Rabani, E. & Javey, A. Inhibited nonradiative decay at all exciton densities in monolayer semiconductors. *Science* **373**, 448–452 (2021).
15. Uddin, S. Z., Higashitarumizu, N., Kim, H., Rahman, I. & Javey, A. Efficiency roll-off free electroluminescence from monolayer WSe_2. *Nano Lett.* **22**, 5316–5321 (2022).
16. Aslan, B., Deng, M. & Heinz, T. F. Strain tuning of excitons in monolayer WSe_2. *Phys. Rev. B* **98**, 115308 (2018).
17. Lien, D. H. et al. Large-area and bright pulsed electroluminescence in monolayer semiconductors. *Nat. Commun.* **9**, 1229 (2018).
18. Baugher, B., Churchill, H., Yang, Y. & Pablo, J. Optoelectronic devices based on electrically tunable p–n diodes in a monolayer dichalcogenide. *Nat. Nanotechnol.* **9**, 262–267 (2014).
19. Pospischil, A., Furchi, M. & Mueller, T. Solar-energy conversion and light emission in an atomic monolayer p–n diode. *Nat. Nanotechnol.* **9**, 257–261 (2014).
20. Wang, S. et al. Efficient carrier-to-exciton conversion in field emission tunnel diodes based on MIS-type van der Waals heterostack. *Nano Lett.* **17**, 5156–5162 (2017).
21. Li, D. et al. Electric-field-induced strong enhancement of electroluminescence in multilayer molybdenum disulfide. *Nat. Commun.* **6**, 7509 (2015).
22. Zhang, Y. J., Oka, T., Suzuki, R., Ye, J. T. & Iwasa, Y. Electrically switchable chiral light-emitting transistor. *Science* **344**, 725–728 (2014).
23. Zhang, L. et al. 2D atomic crystal molecular superlattices by soft plasma intercalation. *Nat. Commun.* **11**, 5960 (2020).
24. Windom, B., Sawyer, W. G. & Hahn, D. W. A Raman spectroscopic study of MoS_2 and MoO_3: applications to tribological systems. *Tribol. Lett.* **42**, 301–310 (2011).
25. Petersson, L. G. & Karlsson, S. E. Clean and oxygen exposed potassium studied by photoelectron spectroscopy. *Phys. Scr.* **16**, 425–431 (1977).
26. Kim, Y. S. et al. Atomic-layer-confined multiple quantum wells enabled by monolithic bandgap engineering of transition metal dichalcogenides. *Sci. Adv.* **7**, eabd7921 (2021).
27. Dhall, R. et al. Direct bandgap transition in many-layer MoS_2 by plasma-induced layer decoupling. *Adv. Mater.* **27**, 1573–1578 (2015).
28. Luo, Z. Y. et al. Photoluminescence lightening: extraordinary oxygen modulated dynamics in WS_2 monolayers. *Nano Lett.* **22**, 2112–2119 (2022).
29. Roy, S. et al. Atomic observation of filling vacancies in monolayer transition metal sulfides by chemically sourced sulfur atoms. *Nano Lett.* **18**, 4523–4530 (2018).
30. Lien, D. H. et al. Electrical suppression of all nonradiative recombination pathways in monolayer semiconductors. *Science* **364**, 468–471 (2019).
31. Zheng, B. et al. WO_3-WS_2 vertical bilayer heterostructures with high photoluminescence quantum yield. *J. Am. Chem. Soc.* **141**, 11754–11758 (2019).
32. Zheng, T. et al. Photoluminescence enhancement at a high generation rate induced by exciton localization. *Opt. Lett.* **46**, 2774–2777 (2021).
33. Kumar, N. et al. Exciton-exciton annihilation in $MoSe_2$ monolayers. *Phys. Rev. B* **89**, 125427 (2014).
34. Uddin, S. Z. et al. Enhanced neutral exciton diffusion in monolayer WS_2 by exciton-exciton annihilation. *ACS Nano* **16**, 8005–8011 (2022).
35. Li, Y. et al. Measurement of the optical dielectric function of monolayer transition-metal dichalcogenides: MoS_2, $MoSe_2$, WS_2, and WSe_2. *Phys. Rev. B* **90**, 205422 (2014).
36. Gonzalez, J. M. & Oleynik, I. I. Layer-dependent properties of SnS_2 and $SnSe_2$ two-dimensional materials. *Phys. Rev. B* **94**, 125443 (2016).
37. Uddin, S. Z. et al. Neutral exciton diffusion in monolayer MoS_2. *ACS Nano* **14**, 13433–13440 (2020).
38. Zhao, Y. et al. A generic electroluminescent device for emission from infrared to ultraviolet wavelengths. *Nat. Electron.* **3**, 612–621 (2020).
39. Paur, M. et al. Electroluminescence from multi-particle exciton complexes in transition metal dichalcogenide semiconductors. *Nat. Commun.* **10**, 1709 (2019).
40. Wang, V. & Javey, A. A resonantly driven, electroluminescent metal oxide semiconductor capacitor with high power efficiency. *ACS Nano* **15**, 15210–15217 (2021).
41. Withers, F. et al. WSe_2 light-emitting tunneling transistors with enhanced brightness at room temperature. *Nano Lett.* **15**, 8223–8228 (2015).
42. Withers, F. et al. Light-emitting diodes by band-structure engineering in van der Waals heterostructures. *Nat. Mater.* **14**, 301–306 (2015).
43. Kresse, G. & Furthmüller, J. Efficient iterative schemes for ab initio total-energy calculations using a plane-wave basis set. *Phys. Rev. B* **54**, 11169–11186 (1996).
44. Kresse, G. & Furthmüller, J. Efficiency of ab-initio total energy calculations for metals and semiconductors using a plane-wave basis set. *Comput. Mater. Sci.* **6**, 15–50 (1996).
45. Perdew, J. P., Burke, K. & Ernzerhof, M. Generalized gradient approximation made simple. *Phys. Rev. Lett.* **77**, 3865–3868 (1996).
46. Grimme, S., Antony, J., Ehrlich, S. & Krieg, H. A consistent and accurate ab initio parametrization of density functional dispersion correction (DFT-D) for the 94 elements H-Pu. *J. Chem. Phys.* **132**, 154104 (2010).
47. Fu, Q. et al. One-step exfoliation method for plasmonic activation of large-area 2D crystals. *Adv. Sci.* **9**, 2204247 (2022).
48. Wang, S. X. et al. Stacking-engineered heterostructures in transition metal dichalcogenides. *Adv. Mater.* **33**, 2005735 (2021).
49. Huang, Y. et al. Universal mechanical exfoliation of large-area 2D crystals. *Nat. Commun.* **11**, 2453 (2020).
50. Ross, J. S. et al. Electrically tunable excitonic light-emitting diodes based on monolayer WSe_2 p–n junctions. *Nat. Nanotechnol.* **9**, 268–272 (2014).
51. Uddin, S. Z., Higashitarumizu, N., Kim, H., Rabani, E. & Javey, A. Engineering exciton recombination pathways in bilayer WSe_2 for bright luminescence. *ACS Nano* **16**, 1339–1345 (2022).

Acknowledgements
J.P.L. acknowledges the National Key Research and Development Program of China (Grant No. 2023YFB3611400) and the National Natural Science Foundation of China (Grant No. 62174026). Z.H.N. acknowledges the National Natural Science Foundation of China (Grant Nos. 62225404, 61927808 and T2321002) and a major project of the Natural Science Foundation of Jiangsu Province (Grant Nos. BK20222007 and BK20232044). Q.Z. acknowledges the National Natural Science Foundation of China (Grant Nos. 12304465 and 62320106004), the Natural Science Foundation of Jiangsu Province (Grant No. BK20230831) and the National Key Research and Development Program of China (Grant No. 2022YFF0609801). J.K.W.Y. acknowledges support from RIE2025 MTC Programmatic Grant No. M21J9b0085 and the Singapore University of Technology and Design through the Kickstarter Initiative (SKI 2021-04-12). Y.J.Z. acknowledges support from the National Natural Science Foundation of China (Grant No. 12004057) and the Natural Science Foundation of Chongqing (Grant No. CSTB2022NSCQ-MSX1183). K.W. and T.T. acknowledge support from the Japan Society for the Promotion of Science (KAKENHI Grant Nos. 21H05233 and 23H02052) and the World Premier International Research Center Initiative, Ministry of Education, Culture, Sports, Science and Technology, Japan. We thank Y. Zhao (ShanghaiTech University) for a helpful discussion on the transient LEDs. We thank H. Nan and S. Xiao (Jiangnan University) for a fruitful discussion on the plasma instrument. We thank Z. Han (Shanxi University) for a helpful discussion on FET transportation. We also thank X. Wang, Y. Xiong and J. Yao for helpful discussions regarding the KPFM measurements.

Author contributions
Q.Z., J.P.L. and Z.H.N. supervised the project. Q.Z. designed the experiments, analysed the data, and wrote and revised the paper. S.X.W. conceived and performed the experiments, wrote and revised the paper, and analysed the optical data. Q.F. performed the FET and LED experiments, analysed the electrical data, contributed to drafting and revising the paper, and supervised the experiments. T. Zheng performed the optical pump–probe measurements. X.H. and Y.H. drew the schematic diagrams. H.W. and J.K.W.Y. performed the dielectric modelling calculations. T. Zhou and Y.W.Z. participated in debugging the time-resolved testing system. T.Q.L. provided the substrate for the EL device. J.L. and Z.X.D. performed the hBN encapsulation. X.Z., K.Q.C., Y.W.X., T.X. and L.T.S. performed the cross-sectional TEM measurements. J.H.H. performed the STEM measurements. Y.J.Z. performed the density functional theory calculations. Y.M.Y. performed the KPFM measurements. Z.L.H., Q.X.W. and J.X.Y. provided advice regarding the paper. K.W. and T.T. provided high-quality hBN.

Competing interests
The authors declare no competing interests.

Additional information
Supplementary information The online version contains supplementary material available at https://doi.org/10.1038/s41928-024-01264-3.

Correspondence and requests for materials should be addressed to Qi Zhang, Junpeng Lu or Zhenhua Ni.

Peer review information *Nature Electronics* thanks Anlian Pan, Yasuhiro Yamada and the other, anonymous, reviewer(s) for their contribution to the peer review of this work.

Reprints and permissions information is available at www.nature.com/reprints.

Publisher's note Springer Nature remains neutral with regard to jurisdictional claims in published maps and institutional affiliations.

[1]Key Laboratory of Quantum Materials and Devices of Ministry of Education, School of Physics, Southeast University, Nanjing, China. [2]Advanced Research Institute of Multidisciplinary Science, Beijing Institute of Technology, Beijing, China. [3]Engineering Product Development Pillar, Singapore University of Technology and Design, Singapore, Singapore. [4]SEU-FEI Nano-Pico Center, Key Laboratory of MEMS of Ministry of Education, Southeast University, Nanjing, China. [5]College of Physical Science and Technology, Xiamen University, Xiamen, China. [6]Institute for Functional Intelligent Materials, National University of Singapore, Singapore, Singapore. [7]Research Center for Electronic and Optical Materials, National Institute for Materials Science, Tsukuba, Japan. [8]Research Center for Materials Nanoarchitectonics, National Institute for Materials Science, Tsukuba, Japan. [9]Changchun Institute of Optics, Fine Mechanics and Physics, Chinese Academy of Sciences, Changchun, China. [10]College of Materials Science and Engineering, Hunan University, Changsha, China. [11]National Innovation Center for Industry-Education Integration of Energy Storage Technology, MOE Key Laboratory of Low-Grade Energy Utilization Technologies and Systems, CQU-NUS Renewable Energy Materials & Devices Joint Laboratory, School of Energy & Power Engineering, Chongqing University, Chongqing, China. [12]School of Chemistry and Chemical Engineering, Southeast University, Nanjing, China. [13]School of Electronic Science & Engineering, Southeast University, Nanjing, China. [14]Purple Mountain Laboratories, Nanjing, China. [15]These authors contributed equally: Shixuan Wang, Qiang Fu. ✉e-mail: zhangxinyunqi@seu.edu.cn; phyljp@seu.edu.cn; zhni@seu.edu.cn